

Spatially modulated superconductivity in the Kagome Hubbard model

Tilman Schwemmer,^{1,2,*} Hendrik Hohmann,^{1,2,*} Matteo Dürrnagel,^{1,2,3,*} Janik Potten,^{1,2} Jacob Beyer,^{1,4,5,6} Stephan Rachel,⁴ Yi-Ming Wu,⁷ Srinivas Raghu,⁷ Tobias Müller,^{1,2} Werner Hanke,^{1,2} and Ronny Thomale^{1,2,8,†}

¹*Institute for Theoretical Physics, Julius-Maximilians-Universität Würzburg, 97074 Würzburg, Germany*

²*Würzburg-Dresden Cluster of Excellence ct.qmat, Univ. of Würzburg, 97074 Würzburg, Germany*

³*Institute for Theoretical Physics, ETH Zürich, 8093 Zürich, Switzerland*

⁴*School of Physics, University of Melbourne, Parkville, VIC 3010, Australia*

⁵*Institute for Theoretical Solid State Physics, RWTH Aachen University, 52062 Aachen, Germany*

⁶*JARA Fundamentals of Future Information Technology, 52062 Aachen, Germany*

⁷*Stanford Institute for Theoretical Physics, Stanford University, Stanford, California 94305, USA*

⁸*Department of Physics and Quantum Centers in Diamond and Emerging Materials (QuCenDiEM) group, Indian Institute of Technology Madras, Chennai 600036, India*

(Dated: March 4, 2024)

We identify a superconducting order featuring spatial pair modulations on the kagome lattice subject to onsite Hubbard U and nearest neighbor V interactions. Within our functional renormalization group analysis, this state appears with a concomitant d -wave superconducting (SC) instability at zero lattice momentum, where it distinguishes itself through *intra-unit cell modulations* of the pairing function thus breaking the discrete space group symmetry. The relative weight of the sublattice modulated superconductor (SMS) and d -wave SC is influenced by the absolute interaction strength and coupling ratio V/U . Parametrically adjacent to this domain at weak coupling, we find an intra-unit cell modulated vestigial charge density wave and an s -wave SC instability. Our study provides a microscopic setting and thorough description of this novel SMS arising within a translation symmetry broken background.

Introduction. Superconducting (SC) order beyond spatially uniform pairing is a longstanding area of condensed matter research [1]. The idea of a pair density wave (PDW), i.e., spatially varying electron pairing manifesting either as finite range fluctuations or long range order has attained significant attention in the context of high- T_c cuprates [2]. There, intriguing phenomena such as Fermi arcs or layer decoupling find a rather intuitive explanation from the viewpoint of a PDW reference state. Most recently, PDWs have surfaced in experimental signatures for a plethora of material classes like kagome metals, transition-metal dichalcogenides, heavy-fermion compound UTe_2 and pnictides [3–7], evoking a universality of the PDW state in correlated electron systems. As tempting and rich as the principal phenomenology might be, the microscopic evidence for a PDW state still is rather poor. Spatially modulated SC pairing has only been rigorously accessed in the Fulde-Ferrell-Larkin-Ovchinnikov (FFLO) scenario of subjecting weak coupling spin-singlet SC to a magnetic field [8, 9]. Without an external field, there is no generic weak coupling solution featuring Cooper pairs at finite lattice momentum. Therefore, the majority of previous attempts had to resort to effective mean field treatments either through postulating finite range bare pair hopping [10] or analyzing higher order terms of Ginzburg Landau expansions [11–13]. It is then usually a matter of non-universal parameter choice whether one finds a PDW as competing order

to uniform SC and charge density wave (CDW), or as a, possibly fluctuating, high-temperature mother state yielding vestigial SC and CDW order at lower temperature [1]. It is thus of central interest to identify a microscopic approach to correlated electron systems that realizes a PDW state [15]. The functional renormalization group (FRG) [16, 17] suggests itself as a natural method to access ordering instabilities at and beyond weak coupling. Even though it lacks an analytical control parameter which is the archetypal challenge for any order at intermediate coupling, the FRG treats all bilinear fermionic orders on equal footing and allows for a smooth interpolation to the weak coupling limit by reducing the interaction strength. FRG calculations were demonstrated to adequately describe even intricate phase diagrams of multi-orbital correlated electron systems such as iron pnictides [18, 19]. As a guiding motif for our study of spatially modulated superconductors we identify the non-trivial sublattice structure of experimentally observed PDW materials. This suggests the U - V kagome Hubbard model (KHM), where U and V denote the onsite and nearest neighbor (NN) electronic repulsion on the kagome lattice, respectively, as a blueprint to examine the sublattice structure of the low energy fluctuations and its imprint on emergent exotic electronic orders [20, 21]. In particular, the geometry of the KHM promotes sublattice interference (SI) [14], leading to pronounced non-local interactions and emergent NN pair hopping, which creates a propensity for PDW formation [22].

Moreover, the sublattice degree of freedom allows for a formation of intra-unit cell modulated states. In analog

* These authors contributed equally.

† Corresponding author: rthomale@physik.uni-wuerzburg.de

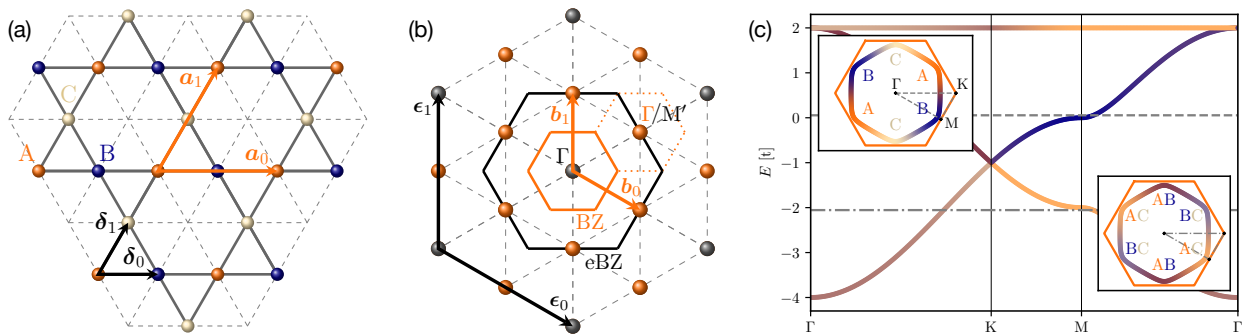


FIG. 1. Kagome Fermiology and extended zone scheme. (a) Kagome lattice with sublattices A , B , and C along with the inter $\mathbf{a}_{0,1}$ and intra $\delta_{0,1}$ unit cell vectors. (b) Fourier transform of the kagome lattice with Brillouin zone (BZ) in orange and extended Brillouin zone in black. M' points in the eBZ coincide with the Γ point in the BZ. (c) The kagome band structure features a flat band and two dispersive bands which display particular eigenstate sublattice distribution according to sublattice interference [14]. p-type (m-type) van Hove fillings are symbolized by dashed (dashed-dotted) lines.

to an intra-unit cell modulated charge density wave we observe a superconducting state of equal pair modulation periodicity, that hence features similar phenomenology to a PDW. However, this state does not break an additional translation symmetry but rotational symmetry within the unit cell and hence surfaces as a $\mathbf{Q} = 0$ instability in the BZ. As this deviates from the common definition of PDW, we label the obtained instability *sublattice modulated superconductivity* (SMS).

In this Letter, we develop a theory for an SMS state observed within FRG calculations. In particular, the state we find does not appear as a parasitic onset order to another electronic instability, but unfolds as part of the leading instability in the particle-particle (pp) channel descending from a pristine kagome metallic state. In terms of symmetry classification at the pp instability level, it admixes with inplane d -wave SC (d SC) in the E_2 irreducible representation of the hexagonal point group C_{6v} . The key to disentangle the SMS from the d SC contribution is the center of mass dependence of the condensate wave function in the tri-atomic unit cell basis. Here, the SMS component exhibits intra-unit cell modulations while the d SC component is uniform.

Kagome Hubbard model (KHM). We start from

$$H = t \sum_{\langle i,j \rangle} (c_{i\sigma}^\dagger c_{j\sigma} + \text{h.c.}) + U \sum_{i=1}^N n_{i\uparrow} n_{i\downarrow} + \frac{V}{2} \sum_{\langle i,j \rangle; \sigma\sigma'} n_{i\sigma} n_{j\sigma'}, \quad (1)$$

where $c_{i\sigma}^\dagger, c_{i\sigma}$ denote electron creation and annihilation operators at site i with spin σ , $n_{i\sigma} = c_{i\sigma}^\dagger c_{i\sigma}$, and t , U , and V denote the energy scales of hopping, onsite Hubbard, and NN repulsion, respectively. The kagome lattice depicted in Figure 1a features a non-bipartite lattice of corner-sharing triangles, resulting in three sublattices A , B , and C as well as Bravais lattice vectors \mathbf{a}_0 and \mathbf{a}_1 . Alternatively, it can be interpreted as a charge density wave formation at $3/4$ filling of an un-

derlying triangular lattice with halved unitcell vectors δ_0 and δ_1 , where every fourth unoccupied site is projected out. In reciprocal space (Figure 1b), this corresponds to the reduced (orange) and extended (black) Brillouin zone (BZ) spanned by the vectors $\mathbf{b}_{0,1}$ and $\boldsymbol{\epsilon}_{0,1}$ according to $\mathbf{b}_i^\top \mathbf{a}_j = \boldsymbol{\epsilon}_i^\top \boldsymbol{\delta}_j = 2\pi\delta_{ij}$. The three inequivalent van Hove points at the M points in the BZ epitomize a peculiar density of states of differing sublattice occupancy (pure p-type at filling $n = 5/12$ for the upper and mixed m-type ($n = 3/12$) for the lower van Hove level in Figure 1c) [14, 23], a generic feature of kagome metals which has been recently confirmed by angle-resolved photoemission spectroscopy (ARPES) [24, 25]. For both m-type and p-type, the mismatch of sublattice support for electronic eigenstates connected by van Hove point nesting triggers SI.

FRG instability analysis. The FRG formulates an ultraviolet to infrared cutoff flow of the two-particle electronic vertex operator $V(\mathbf{k}_1, \mathbf{k}_2, \mathbf{k}_3, \mathbf{k}_4) c_{\mathbf{k}_4}^\dagger c_{\mathbf{k}_3}^\dagger c_{\mathbf{k}_2} c_{\mathbf{k}_1}$, as a set of differential equations, where the \mathbf{k}_i denote lattice momenta. We employ the FRG in its truncated unity (TU) approximation, where the vertex is separated into three different contributions according to their distinctive transfer momenta [26], which can be classified as two particle-hole (ph) and a single particle-particle (pp) channel. The complementary vertex momenta are expanded in plane wave formfactors $\phi_f(\mathbf{k}) = e^{i\mathbf{r}_f \cdot \mathbf{k}}$ via the Bravais lattice sites $\mathbf{r}_f = n\mathbf{a}_0 + m\mathbf{a}_1$, $n, m \in \mathbb{Z}$. For the KHM, any channel vertex function is specified by a 4-tuple of sublattice indices $\{o_i\}$, $i = 1, 2, 3, 4$, transfer momentum \mathbf{Q} , and two residual momenta which we expand into formfactors according to

$$\mathcal{V}_{ff'}^{\{o_i\}}(\mathbf{Q}) = \int_{\text{BZ}} d\mathbf{k} d\mathbf{k}' V^{\{o_i\}}(\mathbf{Q}, \mathbf{k}, \mathbf{k}') \phi_f(\mathbf{k}) \bar{\phi}_{f'}(\mathbf{k}'). \quad (2)$$

Truncating the set of basis functions, reflecting the locality of pp and ph pairs, this unitary expansion be-

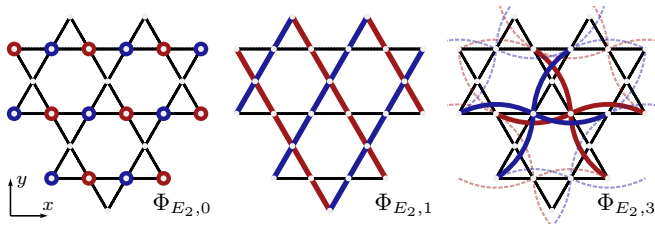


FIG. 2. Harmonics of the E_2 irrep with y -mirror eigenvalue -1 . We show the onsite ($\Phi_{E_2,0}$), first NN ($\Phi_{E_2,1}$), and third NN harmonic ($\Phi_{E_2,3}$). We skip the second NN due to its similarity to the first NN. Red/blue indicates positive/negative value of the pair correlation Eq. (4) between connected sites.

comes approximate. We terminate the flow at an energy scale Λ_c , upon encountering a divergence in a vertex element indicating a symmetry breaking phase transition. At this point, the effective vertex contains all higher energy quantum fluctuations accessible within the FRG approach. For SC pairing at $\mathbf{Q} = 0$, the system's ground state is then obtained from the BCS gap equation which reduces to an eigenvalue problem

$$\lambda \Delta_{o_1 o_2}^f = \sum_{f' o_3 o_4} \mathcal{V}_{f f'}^{\{o_i\}}(0) \Delta_{o_3 o_4}^{f'} \quad (3)$$

at the onset of ordering. The functional form of the SC order parameter is thus given by the eigenstate $\Delta_{o_1 o_2}^f$ associated with the most negative eigenvalue λ . Exploiting the group symmetry constraints on Eq. (3) along Schur's lemma allows for a classification of $\Delta_{o_1 o_2}^f$ in terms of irreducible representations (irreps) of C_{6v} . Within our TUFGRG analysis, we identify an extended region in the U - V parameter space where $\mathbf{Q} = 0$ instabilities in the spin-singlet pp channel dominate, and the superconducting order parameter transforms according to the E_2 irrep.

Classification of the E_2 pp instability. A two-electron expectation value in the spin singlet sector

$$\langle c_{\mathbf{r}_i, \uparrow}^\dagger c_{\mathbf{r}_j, \downarrow}^\dagger - c_{\mathbf{r}_i, \downarrow}^\dagger c_{\mathbf{r}_j, \uparrow}^\dagger \rangle = \delta_{\mathbf{r}_i, \rho} \delta_{\mathbf{r}_j, \rho} \Phi(\mathbf{r}_i, \mathbf{r}_j) \quad (4)$$

is most conveniently described in terms of a center of mass coordinate (CMC) $\mathbf{R} = (\mathbf{r}_i + \mathbf{r}_j)/2$ and a relative coordinate (RC) $\mathbf{r} = \mathbf{r}_i - \mathbf{r}_j$. In the following, we denote the set of all lattice points by ρ and use ρ_o for points related to sublattice $o \in \{A, B, C\}$. We introduce $\mathbf{a}_2 = \mathbf{a}_1 - \mathbf{a}_0$ and $\delta_2 = \delta_1 - \delta_0$ for notational convenience. Since the kagome lattice is not of Bravais type, the directions of NN bonds depend on the sublattice. For each pairing distance, i.e., each value of the RC (onsite, NN, etc.), the E_2 irrep is expanded in pairs of degenerate orthogonal states, characterized by even or odd transformation behavior under mirror symmetry along the y -axis [26]. We order different E_2 candidate states by their RC length and constrain ourselves to the mirror-odd state as we present a graphical representation in Figure 11. The on-

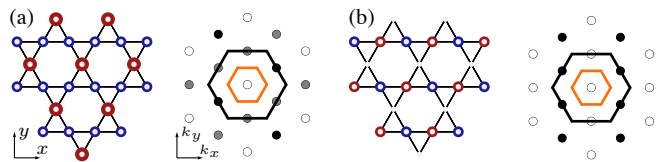


FIG. 3. Real space representation of the two onsite pairing wavefunction with E_2 symmetry and their Cooper pair momentum structure in the eBZ. Lighter shading corresponds to less intensity. Contrarily to the d SC pairing wavefunctions of Eq. (6), finite Cooper pair momentum is revealed by the unfolding into the eBZ [26]. The depicted \mathbf{Q} structure resembles the expected STM signature of the SMS state.

site ($\mathbf{r} = 0$) pairing wave function reads

$$\Phi_{E_2,0}(\mathbf{R}, \mathbf{r}) = \left(\delta_{\mathbf{R}, \rho_A} - \delta_{\mathbf{R}, \rho_B} \right) \delta_{\mathbf{r}, \mathbf{0}}. \quad (5)$$

The absence of a lattice site at the point group's rotation center, allows for such onsite pairing wave functions on any non-Bravais lattice. The trivial transformation property of the RC is complemented by a non-trivial CMC function due to the reduced site symmetry group of the $3c$ Wyckoff position. In contrast, the NN pairing state

$$\Phi_{E_2,1}(\mathbf{R}, \mathbf{r}) = \delta_{\mathbf{r}, \pm \delta_1} - \delta_{\mathbf{r}, \pm \delta_2} \quad (6)$$

features a trivial CMC dependence, and instead it is the RC that captures the E_2 transformation behaviour. Whereas the second NN state is structurally equivalent [26] to the NN state, the third NN pairing reads

$$\begin{aligned} \Phi_{E_2,3}(\mathbf{R}, \mathbf{r}) = & \delta_{\mathbf{R}, \rho_B} \delta_{\mathbf{r}, \pm \mathbf{a}_0} - \delta_{\mathbf{R}, \rho_A} \delta_{\mathbf{r}, \pm \mathbf{a}_0} \\ & + \delta_{\mathbf{R}, \rho_C} \left(\delta_{\mathbf{r}, \pm \mathbf{a}_1} - \delta_{\mathbf{r}, \pm \mathbf{a}_2} \right). \end{aligned} \quad (7)$$

It cannot be decomposed into a product of solely CMC and RC dependent functions. This stems from two symmetry-inequivalent types of third NN on the kagome lattice due to the reduced C_{2v} site symmetry group, that yields the additional spatial CMC structure [26].

SMS wave function. Two candidate states may belong to the same irrep and yet trace back to entirely different physical origins. For the A_1 pairing irrep on the square lattice, this has been extensively discussed in the context of s_{\pm} vs. s_{++} -wave SC in iron pnictides [27, 28]. For the kagome lattice, the fundamentally different nature of E_2 formfactors becomes apparent upon disentangling the spatial information encoded in CMC and RC, respectively. The Cooper pair wave function of typical zero momentum SCs features a uniform CMC dependence, while the RC encodes the transformation behavior of the associated irrep. Eq. (5), however, describes a scenario where the typical roles of CMC and RC are interchanged. It obeys $\sum_{\mathbf{R}} \Phi(\mathbf{R}, \mathbf{r}) = 0$, which is a characteristic of PDW-type pairing [29]. The key point to appreciate here is that

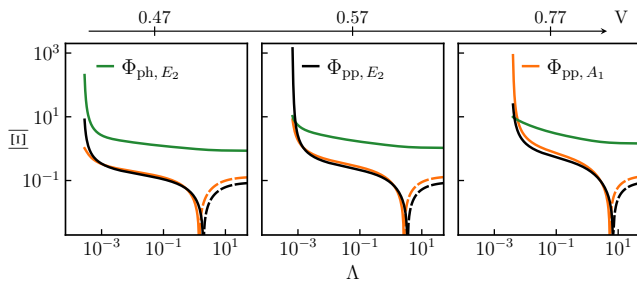


FIG. 4. FRG vertex analysis for $U/t = 0.14$ and $0.47 < V/t < 0.77$ as a function of the energy cutoff Λ . E_2 CDW (Φ_{ph, E_2} , green), SMS E_2 pp order (Φ_{pp, E_2} , black), and SC A_1 pp (Φ_{pp, A_1} , orange) compete for the leading instability. Attractive (repulsive) expectation values $|\Xi|$ of the leading instabilities at Λ_c are indicated by solid (dashed) lines [26].

despite the $\mathbf{Q} = 0$ channel, *spatially modulated contributions can be distinguished from homogeneous ones within the multi-site unit cell*. This is the essential difference between the SMS and d SC contributions to an E_2 pp instability in the KHM.

Restoring the full real space information previously encoded in the sublattice indices of the tri-atomic basis by transferring the SMS state of Eq. (5) to the extended BZ shown in Fig. 3 reveals finite momentum Cooper pairing, that can be directly attributed to a generalised version of the structure factor experimentally accessible in STM measurements (for details cf. SM [26]): By locally probing the differential conductance via the Josephson tunneling signal of a superconducting STM tip, the SC gap can be monitored with high spatial resolution. The Fourier transform of the pairing gap maps exhibits peaks at the wave vectors associated with the Cooper pair modulation, that can be matched with the peak structure in Fig. 3. This allows for a clear experimental distinction between the proposed SMS state and uniform SC pairing [30–32].

SMS phase domain. Within our TUFGRG analysis of the KHM, the E_2 pp instability domain is governed by intra-sublattice pairing, i.e., the eigenstates of Eq. (3) are described by a linear combination of $\Phi_{E_2,0}$ and $\Phi_{E_2,3}$ [26]. This allows to identify the E_2 pp instability as a SMS. Such states were previously found, yet not adequately appreciated in the kagome phase diagram of Ref. 21 and 33. The intra-sublattice pairing tendency can be understood from the viewpoint of SI: Under the RG, effects of U are suppressed while V grows [22], making inter-sublattice pairing less favourable. This trend also manifests in the fact that the SMS instability at small U/t is parametrically framed by an E_2 -type CDW and an A_1 -type, i.e., s -wave SC (Figure 4) at p-type van Hove filling.

The SMS state emerges as interstitial order via competing interaction processes projected into the pairing channel: U drives non-local spin fluctuations; V , by con-

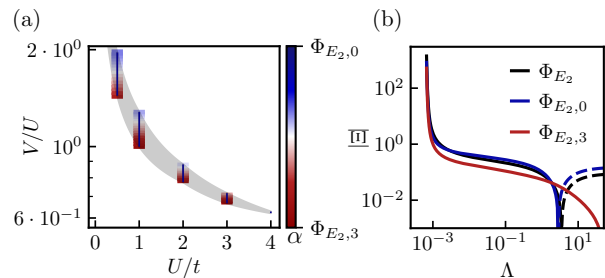


FIG. 5. (a) Admixture ratio α of $\Phi_{E_2,0}$ (blue) (5) and $\Phi_{E_2,3}$ (red) (7) for the E_2 pp domain at p-type van Hove filling ($n = 5/12$). (b) Expectation value of the leading eigenstate at Λ_c (black), $\Phi_{E_2,0}$, and $\Phi_{E_2,3}$. Negative (positive) values are indicated by solid (dashed) lines.

trast, generates charge fluctuations entering the Cooper channel as onsite attractive interactions [34]. In Figure 4, we illustrate the generic scenario of competing instabilities generated by this interplay of local and non-local interactions by comparing FRG flows for varying bare values $0.47 < V < 0.77$ at fixed $U = 0.14$, i.e., located in the weak coupling domain. Both SMS-type and s -wave SC channels are initially repulsive (dashed lines) and subsequently turn attractive (solid lines) through the RG flow. Remarkably, the adjacent CDW features the same irrep and intra-sublattice modulation as the SMS phase, suggesting vestigial symmetry-type restoration at the phase transition. In previous contexts, PDW fluctuations were similarly found to predominantly occur around phase transitions between a density wave phase and SC pairing, where a variety of competing and/or cooperative orders arise at intermediate coupling strength [1]. Any weak coupling theory of PDW has hitherto relied on fine-tuned Fermiology [35]. Here, however, we find that the SMS prevails beyond p-type van Hove filling whenever intra-unit cell modulations become competitive to homogeneous pairing functions due to SI.

The competition of interaction processes is directly reflected in the pairing wave functions overlap with $\Phi_{E_2,0}$ and $\Phi_{E_2,3}$ [26] and their relative weight α , which is depicted in Figure 5a for the SMS regime at p-type van Hove filling. Doping slightly away from this point significantly increases the SMS region, e.g. by a factor of ≈ 2.5 for $U = 3$ at $n = 1.01 \times 5/12$. The third NN state $\Phi_{E_2,3}$ does not suffer an energy penalty from U in (1) and thus promotes attractive pairing channel already at bare coupling (Figure 5b). Analogous to the previous discussion, V -driven intra-unit cell charge fluctuations yield an onsite attraction of Cooper pairs through the RG flow [21]. The onsite contribution $\Phi_{E_2,0}$ to SMS increases with V , and eventually drives the system into an s -wave SC.

Conclusion and outlook. Our findings emphasize the fundamental role of the sublattice texture on the Fermi surface in a microscopic theory of spatially modulated

pairing, a motif also shared among the different PDW candidates [35–37]. The new type of sublattice modulated SC instability we find for the KHM model is facilitated by the nontrivial basis in the unit cell. This allows spatial modulations of the Cooper pair wave function, while still exploiting the Cooper logarithm of a $\mathbf{Q} = 0$ pairing instability as main driver for the symmetry breaking transition. This establishes the proposed type of SMS as a generic instability of a Fermi liquid with sublattice degrees of freedom and may explain the broad range of materials exhibiting PDW phenomenology. The breaking of rotational symmetry instead of translational symmetry by intra-unit cell modulations of the SC order parameter finds a direct correspondence for magnetically ordered systems in the new field of altermagnetism [38, 39]. Viewing the kagome lattice as a fictitious $3/4$ filling CDW of an underlying triangular lattice (Figure 1a), we recover the expected intertwined character of PDW: the kagome-CDW at $2\delta_{1,0}$ comes along with a $2\delta_{1,0}$ PDW competing with d SC. This motif carries over to SC within the 2×2 charge order in 135 kagome compounds [3, 36]: Spatially modulated intra-unit cell SC can arise within the enlarged 2×2 unit cell in the charge ordered phase without an additional translation symmetry breaking imposed by the SC transition. Within the SMS phase, experimental signatures of PDW like reciprocal Josephson effect can still be observed [41–43]. To target experimentally observed PDW states in kagome compounds like the roton density wave reported for CsV_3Sb_5 within the charge order domain [3], the methodological shortcoming to surmount in the future is to continue the FRG flow throughout the preceding charge ordered phases [40].

Acknowledgement. We thank S. A. Kivelson, M. Klett, J.B. Hauck, and M. Sigrist for discussions. The work is funded by the Deutsche Forschungsgemeinschaft (DFG, German Research Foundation) through Project-ID 258499086 - SFB 1170 and and through the Würzburg-Dresden Cluster of Excellence on Complexity and Topology in Quantum Matter – *ct.qmat* Project-ID 390858490 - EXC 2147. We acknowledge HPC resources provided by the Erlangen National High Performance Computing Center (NHR@FAU) of the Friedrich-Alexander-Universität Erlangen-Nürnberg (FAU). NHR funding is provided by federal and Bavarian state authorities. NHR@FAU hardware is partially funded by the DFG – 440719683. M.D. received funding from the European Research Council under Grant No. 771503 (TopMech-Mat). S.R. was supported in part by the US Department of Energy, Office of Basic Energy Sciences, Division of Materials Sciences and Engineering, under contract number DE-AC02-76SF00515. J.B. thanks the DFG for support through RTG 1995 from SPP 244 “2DMP”.

- [1] D. F. Agterberg, J. S. Davis, S. D. Edkins, E. Fradkin, D. J. Van Harlingen, S. A. Kivelson, P. A. Lee, L. Radzihovsky, J. M. Tranquada, and Y. Wang, The physics of pair-density waves: Cuprate superconductors and beyond, *Annual Review of Condensed Matter Physics* **11**, 231 (2020).
- [2] E. Fradkin, S. A. Kivelson, and J. M. Tranquada, Colloquium: Theory of intertwined orders in high temperature superconductors, *Rev. Mod. Phys.* **87**, 457 (2015).
- [3] H. Chen, H. Yang, B. Hu, Z. Zhao, J. Yuan, Y. Xing, G. Qian, Z. Huang, G. Li, Y. Ye, S. Ma, S. Ni, H. Zhang, Q. Yin, C. Gong, Z. Tu, H. Lei, H. Tan, S. Zhou, C. Shen, X. Dong, B. Yan, Z. Wang, and H.-J. Gao, Roton pair density wave in a strong-coupling kagome superconductor, *Nature* **599**, 222 (2021).
- [4] X. Liu, Y. X. Chong, R. Sharma, and J. C. S. Davis, Discovery of a cooper-pair density wave state in a transition-metal dichalcogenide, *Science* **372**, 1447 (2021).
- [5] Q. Gu, J. P. Carroll, S. Wang, S. Ran, C. Broyles, H. Siddiquee, N. P. Butch, S. R. Saha, J. Paglione, J. C. S. Davis, and X. Liu, Detection of a pair density wave state in uTe_2 , *Nature* **618**, 921 (2023).
- [6] H. Zhao, R. Blackwell, M. Thinel, T. Handa, S. Ishida, X. Zhu, A. Iyo, H. Eisaki, A. N. Pasupathy, and K. Fujita, Smectic pair-density-wave order in $\text{EuRbFe}_4\text{As}_4$, *Nature* **618**, 940 (2023).
- [7] H. Li, D. Oh, M. Kang, H. Zhao, B. R. Ortiz, Y. Oey, S. Fang, Z. Ren, C. Jozwiak, A. Bostwick, E. Rotenberg, J. G. Checkelsky, Z. Wang, S. D. Wilson, R. Comin, and I. Zeljkovic, Small fermi pockets intertwined with charge stripes and pair density wave order in a kagome superconductor (2023), [arXiv:2303.07254 \[cond-mat.supr-con\]](https://arxiv.org/abs/2303.07254).
- [8] P. Fulde and R. A. Ferrell, Superconductivity in a strong spin-exchange field, *Phys. Rev.* **135**, A550 (1964).
- [9] A. I. Larkin and Y. N. Ovchinnikov, *Sov. Phys. JETP* **20**, 762 (1965).
- [10] F. Loder, A. P. Kampf, and T. Kopp, Superconducting state with a finite-momentum pairing mechanism in zero external magnetic field, *Phys. Rev. B* **81**, 020511 (2010).
- [11] E. Berg, E. Fradkin, and S. A. Kivelson, Charge-4e superconductivity from pair-density-wave order in certain high-temperature superconductors, *Nature Physics* **5**, 830 (2009).
- [12] D. F. Agterberg and H. Tsunetsugu, Dislocations and vortices in pair-density-wave superconductors, *Nature Physics* **4**, 639 (2008).
- [13] P. A. Lee, Amperean pairing and the pseudogap phase of cuprate superconductors, *Phys. Rev. X* **4**, 031017 (2014).
- [14] M. L. Kiesel and R. Thomale, Sublattice interference in the kagome hubbard model, *Phys. Rev. B* **86**, 121105 (2012).
- [15] Y.-M. Wu, P. A. Nosov, A. A. Patel, and S. Raghu, Pair density wave order from electron repulsion, *Phys. Rev. Lett.* **130**, 026001 (2023).
- [16] W. Metzner, M. Salmhofer, C. Honerkamp, V. Meden, and K. Schönhammer, Functional renormalization group approach to correlated fermion systems, *Rev. Mod. Phys.* **84**, 299 (2012).
- [17] J. Beyer, J. B. Hauck, and L. Klebl, Reference results for the momentum space functional renormalization group, *The European Physical Journal B* **95**, 65 (2022).

- [18] F. Wang, H. Zhai, Y. Ran, A. Vishwanath, and D.-H. Lee, Functional renormalization-group study of the pairing symmetry and pairing mechanism of the fe-based high-temperature superconductor, *Phys. Rev. Lett.* **102**, 047005 (2009).
- [19] C. Platt, W. Hanke, and R. Thomale, Functional renormalization group for multi-orbital fermi surface instabilities, *Advances in Physics* **62**, 453 (2013).
- [20] M. L. Kiesel, C. Platt, and R. Thomale, Unconventional fermi surface instabilities in the kagome hubbard model, *Phys. Rev. Lett.* **110**, 126405 (2013).
- [21] W.-S. Wang, Z.-Z. Li, Y.-Y. Xiang, and Q.-H. Wang, Competing electronic orders on kagome lattices at van hove filling, *Phys. Rev. B* **87**, 115135 (2013).
- [22] Y.-M. Wu, R. Thomale, and S. Raghu, *Sublattice Interference promotes Pair Density Wave order in Kagome Metals* (2022), arXiv:2211.01388 [cond-mat] type: article.
- [23] X. Wu, T. Schwemmer, T. Müller, A. Consiglio, G. Sangiovanni, D. Di Sante, Y. Iqbal, W. Hanke, A. P. Schnyder, M. M. Denner, M. H. Fischer, T. Neupert, and R. Thomale, Nature of unconventional pairing in the kagome superconductors AV_3Sb_5 ($A=K, Rb, Cs$), *Phys. Rev. Lett.* **127**, 177001 (2021).
- [24] M. Kang, S. Fang, J.-K. Kim, B. R. Ortiz, S. H. Ryu, J. Kim, J. Yoo, G. Sangiovanni, D. Di Sante, B.-G. Park, C. Jozwiak, A. Bostwick, E. Rotenberg, E. Kaxiras, S. D. Wilson, J.-H. Park, and R. Comin, Twofold van Hove singularity and origin of charge order in topological kagome superconductor CsV_3Sb_5 , *Nature Physics* **18**, 301 (2022).
- [25] Y. Hu, X. Wu, B. R. Ortiz, S. Ju, X. Han, J. Ma, N. C. Plumb, M. Radovic, R. Thomale, S. D. Wilson, A. P. Schnyder, and M. Shi, Rich nature of Van Hove singularities in Kagome superconductor CsV_3Sb_5 *Nature Communications* **13**, 2220 (2022).
- [26] See Supplemental Material and references [16, 17, 19, 44–49] therein for details on TUFGR and further E_2 basis states.
- [27] P. J. Hirschfeld, M. M. Korshunov, and I. I. Mazin, Gap symmetry and structure of fe-based superconductors, *Reports on Progress in Physics* **74**, 124508 (2011).
- [28] A. Chubukov, Pairing mechanism in fe-based superconductors, *Annual Review of Condensed Matter Physics* **3**, 57 (2012).
- [29] D. P. Arovas, E. Berg, S. A. Kivelson, and S. Raghu, The hubbard model, *Annual Review of Condensed Matter Physics* **13**, 239 (2022).
- [30] T. Proslir, A. Kohen, Y. Noat, T. Cren, D. Roditchev, and W. Sacks, Probing the superconducting condensate on a nanometer scale, *Europhysics Letters* **73**, 962 (2006).
- [31] H. Kimura, R. P. Barber, S. Ono, Y. Ando, and R. C. Dynes, Josephson scanning tunneling microscopy: A local and direct probe of the superconducting order parameter, *Phys. Rev. B* **80**, 144506 (2009).
- [32] S. Karan, H. Huang, C. Padurariu, B. Kubala, A. Theiler, A. M. Black-Schaffer, G. Morrás, A. L. Yeyati, J. C. Cuevas, J. Ankerhold, K. Kern, and C. R. Ast, Superconducting quantum interference at the atomic scale, *Nature Physics* **18**, 893–898 (2022).
- [33] C. Wen, X. Zhu, Z. Xiao, N. Hao, R. Mondaini, H. Guo, and S. Feng, Superconducting pairing symmetry in the kagome-lattice hubbard model, *Phys. Rev. B* **105**, 075118 (2022).
- [34] A. T. Rømer, S. Bhattacharyya, R. Valentí, M. H. Christensen, and B. M. Andersen, Superconductivity from repulsive interactions on the kagome lattice, *Physical Review B* **106**, 174514 (2022).
- [35] D. Shaffer, F. J. Burnell, and R. M. Fernandes, Weak-Coupling Theory of Pair Density-Wave Instabilities in Transition Metal Dichalcogenides (2022), arXiv:2209.14469.
- [36] W. Z. Zhou S., Fermi pocket, topological pair density wave, and charge-4e and charge-6e superconductivity in kagomé superconductors, *Nature Communications* **13**, 7288 (2022).
- [37] H.-C. Jiang, Pair density wave in the doped three-band hubbard model on two-leg square cylinders, *Phys. Rev. B* **107**, 214504 (2023).
- [38] I. Mazin (The PRX Editors), Editorial: Altermagnetism—a new punch line of fundamental magnetism, *Phys. Rev. X* **12**, 040002 (2022).
- [39] L. Šmejkal, J. Sinova, and T. Jungwirth, Emerging research landscape of altermagnetism, *Phys. Rev. X* **12**, 040501 (2022).
- [40] M. Salmhofer, C. Honerkamp, W. Metzner, and O. Lauscher, Renormalization group flows into phases with broken symmetry, *Progress of Theoretical Physics* **112**, 943 (2004).
- [41] A. Daido, Y. Ikeda, and Y. Yanase, Intrinsic superconducting diode effect, *Phys. Rev. Lett.* **128**, 037001 (2022).
- [42] J. J. He, Y. Tanaka, and N. Nagaosa, A phenomenological theory of superconductor diodes, *New Journal of Physics* **24**, 053014 (2022).
- [43] Y.-M. Wu, Z. Wu, and H. Yao, Pair-density-wave and chiral superconductivity in twisted bilayer transition metal dichalcogenides, *Phys. Rev. Lett.* **130**, 126001 (2023).
- [44] J. Lichtenstein, D. Sánchez de la Peña, D. Rohe, E. Di Napoli, C. Honerkamp, and S. Maier, High-performance functional renormalization group calculations for interacting fermions, *Computer Physics Communications* **213**, 100 (2017).
- [45] G. A. H. Schober, J. Ehrlich, T. Reckling, and C. Honerkamp, Truncated-Unity Functional Renormalization Group for Multiband Systems With Spin-Orbit Coupling, *Frontiers in Physics* **6** (2018).
- [46] W.-S. Wang, Y.-Y. Xiang, Q.-H. Wang, F. Wang, F. Yang, and D.-H. Lee, Functional renormalization group and variational monte carlo studies of the electronic instabilities in graphene near $\frac{1}{4}$ doping, *Phys. Rev. B* **85**, 035414 (2012).
- [47] C. Husemann and M. Salmhofer, Efficient parametrization of the vertex function, Ω scheme, and the t, t' hubbard model at van hove filling, *Phys. Rev. B* **79**, 195125 (2009).
- [48] J. Reiss, D. Rohe, and W. Metzner, Renormalized mean-field analysis of antiferromagnetism and d -wave superconductivity in the two-dimensional hubbard model, *Phys. Rev. B* **75**, 075110 (2007).
- [49] W. Metzner and H. Yamase, Phase stiffness in an antiferromagnetic superconductor, *Phys. Rev. B* **100**, 014504 (2019).

SUPPLEMENTAL MATERIAL

Truncated Unity FRG

While the natural energy scale of the non-interacting theory is determined by the bandwidth of the single particle spectrum, the situation becomes more delicate in the presence of interactions. Interaction effects establish collective ordering phenomena at energy scale several orders of magnitude below the strength of the bare interaction in the initial Hamiltonian due to screening by the non interacting background. To trace down the effective contribution of interactions to the physics at the important energy scales, a variety of renormalization procedures have been developed to incorporate higher order screening processes in the low energy effective theory.

Among these, the functional renormalization group stands out by its unbiased differentiation of phases and is the natural method for the analysis of spatially modulated states of matter like pair density waves (PDW) or sublattice modulated superconducting (SMS) orders as proposed in the manuscript. While we omit the basics of FRG itself by referencing to the literature [16, 19] instead, we want to reintroduce the TUFGRG [44, 45] approximation here: We start out with the integro-differential equation of the functional renormalization group in its SU(2) reduced form: The exact perturbative expansion of the FRG vertex has already been truncated at the two-particle level to make the infinite hierarchy of coupled equations solvable.

We furthermore exploit spin rotational invariance, which allows to consider the opposite spin channel only. The symmetric and antisymmetric part of the thereby obtained effective interaction resembles the singlet and triplet correlations respectively. For brevity we drop the spin and sublattice indices in all following formulae, which we retain as tensor dimensions of the object $V_{\uparrow\uparrow\downarrow\downarrow}^{\sigma_1\sigma_2\sigma_3\sigma_4}(\mathbf{k}_1, \mathbf{k}_2, \mathbf{k}_3)$. The exact order of indices can be inferred from the diagrammatic expression where the shape of the vertices indicates connected sublattices.

We further employ the truncated unity expansion to the FRG which is based on the singular mode

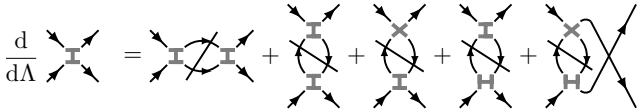


FIG. 6. Diagrammatic representation of the SU(2)-TUFGRG flow. The dash through the pair of propagator lines indicates the derivative w.r.t. the scale Λ . The diagrams can be separated into the three channels by their transfer momentum between the 2-particle vertices: The first diagram is associated with the P -channel, the next three contribute to the D -channel and C -channel consists of the last diagram.

paradigms [46]. To this end the vertex is decomposed in the *particle-particle* (P), *direct particle-hole* (D), *crossed particle-hole* (C) channel

$$V = V_P + V_D + V_C \quad (8)$$

according to the three possible diagrammatic transfer momenta $\mathbf{Q}_P = \mathbf{k}_1 + \mathbf{k}_2$, $\mathbf{Q}_D = \mathbf{k}_1 - \mathbf{k}_3$ and $\mathbf{Q}_C = \mathbf{k}_1 - \mathbf{k}_4$. This primary momentum dependence drives any divergence in the channel, so the remaining spatial dependence of any given function $F(\mathbf{k}_1, \mathbf{k}_2, \mathbf{k}_3)$ can be expanded in a suitable set of formfactors $\phi_f(\mathbf{k})$ via

$$\hat{X}[F]_{ff'}(\mathbf{Q}_X) = \int d\mathbf{k}_X \int d\mathbf{k}'_X \phi_f(\mathbf{k}_X) \phi_{f'}(\mathbf{k}'_X) F(\mathbf{k}_1(\mathbf{Q}_X, \mathbf{k}_X, \mathbf{k}'_X), \mathbf{k}_2(\mathbf{Q}_X, \mathbf{k}_X, \mathbf{k}'_X), \mathbf{k}_3(\mathbf{Q}_X, \mathbf{k}_X, \mathbf{k}'_X)), \quad (9)$$

where $X \in \{P, C, D\}$. Because of the slow-varying nature of the interaction w.r.t. the secondary momenta, the high frequency harmonics can be truncated without significant loss of information. In the present study we choose plane waves $\phi_f(\mathbf{k}) = e^{-i\mathbf{k}\mathbf{r}_f}$ as a complete basis with \mathbf{r}_f representing a Bravais lattice site and consider sites up to third nearest neighbors. By applying the above projection to Figure 6, the RG equation for the vertex

$$\frac{d}{d\Lambda} \hat{X}[\mathcal{V}] = \hat{X}[\dot{\mathcal{V}}_P] + \hat{X}[\dot{\mathcal{V}}_D] + \hat{X}[\dot{\mathcal{V}}_C] \quad (10)$$

breaks down to the three separate channel flow equations

$$\begin{aligned} \hat{P}[\dot{\mathcal{V}}]_{ff'}(\mathbf{Q}_P) &= \sum_{f_1, f_2} \mathcal{V}_{ff_1}(\mathbf{Q}_P) \dot{L}_{f_1 f_2}^{pp}(\mathbf{Q}_P) \mathcal{V}_{f_2 f'}(\mathbf{Q}_P) \\ \hat{D}[\dot{\mathcal{V}}]_{ff'}(\mathbf{Q}_D) &= \sum_{f_1, f_2} \left[-2\mathcal{V}_{ff_1}(\mathbf{Q}_D) \dot{L}_{f_1 f_2}^{ph}(\mathbf{Q}_D) \mathcal{V}_{f_2 f'}(\mathbf{Q}_D) \right. \\ &\quad \left. + \mathcal{V}_{ff_1}(\mathbf{Q}_C) \dot{L}_{f_1 f_2}^{ph}(\mathbf{Q}_D) \mathcal{V}_{f_2 f'}(\mathbf{Q}_D) \right. \\ &\quad \left. + \mathcal{V}_{ff_1}(\mathbf{Q}_D) \dot{L}_{f_1 f_2}^{ph}(\mathbf{Q}_D) \mathcal{V}_{f_2 f'}(\mathbf{Q}_C) \right] \\ \hat{C}[\dot{\mathcal{V}}]_{ff'}(\mathbf{Q}_C) &= \sum_{f_1, f_2} \mathcal{V}_{ff_1}(\mathbf{Q}_C) \dot{L}_{f_1 f_2}^{ph}(\mathbf{Q}_C) \mathcal{V}_{f_2, f'}(\mathbf{Q}_C). \end{aligned} \quad (11)$$

Here $\dot{L}_{ff'}^{pp}(\mathbf{Q})$ and $\dot{L}_{ff'}^{ph}(\mathbf{Q})$ are the product of single-scale propagator and propagator ($\frac{dG^{\Lambda}G^{\Lambda}}{d\Lambda}$) in either particle-particle (pp) or particle-hole (ph) configuration transformed into TU representation.

Since renormalisation effects for each transfer momentum are accumulated separately, the computational complexity of the calculations reduces significantly while retaining momentum conservation which was not possible in the n-patch FRG schemes used previously [19]. Additionally, the full orbital and band space dependencies are kept throughout the RG procedure, since the expansion

in Eq. (9) only effects the momentum quantum numbers. In particular for systems with sublattice, this allows to extract the real space structure within the unit cell from the order parameter at the end of the flow.

We are left with the remaining problem of the cross-channel projections, *i.e.* the contribution of each \dot{V}_X in the two complementary channels. By respecting the interplay between the channels, the TUFGR distinguishes itself from the calculation of three simultaneous but disconnected RPA flows and becomes an unbiased method, which treats propensities towards particle-particle instabilities on equal footing to particle-hole instabilities. The cross channel projections can be reduced to complicated tensor transformations for each pair X, Y from $\{P, C, D\} : X \neq Y$

$$\begin{aligned} d\mathcal{V}_{X,ff'}^{\{o_i\}}(\mathbf{Q}_X) \\ = \sum_{\mathbf{Q}_Y} M_{Y,f_1f_2}^{X,ff'}(\mathbf{Q}_X, \mathbf{Q}_Y) d\mathcal{V}_{Y,f_1f_2}^{\mathcal{P}_{X,Y}\{\{o_i\}\}}(\mathbf{Q}_Y). \end{aligned} \quad (12)$$

This set of integro-differential equations and coupling equations can be integrated as it would be in ordinary FRG:

To obtain a log scale theory close to the Fermi level, we start from the free theory at $\Lambda \sim \infty$ and integrate the flow equations towards lower scale. Upon encountering a phase transition one (or more) of the differentials in Eq. (11) diverges at energy scale Λ_C , which can be related to the critical temperature $T_C \propto \Lambda_C$ of the transition. To associate the divergent channels with physical instabilities, the effective interaction at Λ_C is transformed back into momentum space and decomposed into the pairing

$$\begin{aligned} \Gamma_{pp} = \sum_{\mathbf{Q}\mathbf{k}\mathbf{k}'} \sum_{o_i} V_P^{\{o_i\}}(\mathbf{Q}, \mathbf{k}, \mathbf{k}') \\ c_{\mathbf{k}+\mathbf{Q}/2, o_2 \uparrow}^\dagger c_{-\mathbf{k}+\mathbf{Q}/2, o_3 \downarrow}^\dagger c_{-\mathbf{k}'+\mathbf{Q}/2, o_1 \downarrow} c_{\mathbf{k}'+\mathbf{Q}/2, o_0 \uparrow}, \end{aligned} \quad (13)$$

charge

$$\begin{aligned} \Gamma_{\text{cha}} = \sum_{\mathbf{Q}\mathbf{k}\mathbf{k}'} \sum_{o_i s s'} \left[V_D^{\{o_i\}}(\mathbf{Q}, \mathbf{k}, \mathbf{k}') - \frac{1}{2} V_C^{o_0 o_1 o_3 o_2}(\mathbf{Q}, \mathbf{k}, \mathbf{k}') \right] \\ c_{\mathbf{k}-\mathbf{Q}/2, o_2 s}^\dagger c_{\mathbf{k}+\mathbf{Q}/2, o_0 s}^\dagger c_{\mathbf{k}'+\mathbf{Q}/2, o_3 s'}^\dagger c_{\mathbf{k}'-\mathbf{Q}/2, o_1 s'}, \end{aligned} \quad (14)$$

and magnetic

$$\begin{aligned} \Gamma_{\text{mag}} = \sum_{\mathbf{Q}\mathbf{k}\mathbf{k}'} \sum_{\{o_i\}\{s_i\}} -V_C^{\{o_i\}}(\mathbf{Q}, \mathbf{k}, \mathbf{k}') \sigma_{s_0 s_2}^z \sigma_{s_1 s_3}^z \\ c_{\mathbf{k}'+\mathbf{Q}/2, o_2 s_2}^\dagger c_{\mathbf{k}+\mathbf{Q}/2, o_0 s_0}^\dagger c_{\mathbf{k}-\mathbf{Q}/2, o_3 s_3}^\dagger c_{\mathbf{k}'-\mathbf{Q}/2, o_1 s_1} \end{aligned} \quad (15)$$

contributions [44, 47]. Each renormalized interaction in momentum space is obtained from the quantities in

Eq. (11) via the inverse of Eq. (9), σ^z is the third Pauli matrix. Since the magnetic channel is not further discussed in the weak coupling domain of SMS elaborated on in the main article, “cha” is abbreviated by “ph” for notational convenience.

Mean field analysis

From the effective vertex in the most divergent channel, the functional dependence of the order parameter can be analysed by a subsequent mean field (MF) decomposition of the residual interaction term [19, 48, 49]. Subsequently, we focus on the pairing channel at $\mathbf{Q}_P = 0$, which characterizes uniform superconductivity and sublattice modulated superconductivity. An analogous procedure yields the order parameter of adjacent phases like charge and spin density waves and bond orders.

We start by introducing the non vanishing expectation value

$$\Delta(\mathbf{k}) = \frac{1}{N} \sum_{\mathbf{k}'} \Gamma_P(\mathbf{k}, \mathbf{k}') \langle c_{\downarrow}(-\mathbf{k}') c_{\uparrow}(\mathbf{k}') \rangle \quad (16)$$

with \mathbf{k}, \mathbf{k}' restricted to energy scales below the cutoff, *i.e.* the single particle energies satisfy $|\xi_n(\mathbf{k})| < \Lambda_C \sim 10^{-4}t$. Assuming no accidental band degeneracies at the Fermi level, this allows a unique mapping between momentum and band quantum number and we hence drop the latter one. Neglecting second order fluctuations around the MF solution, the free energy of the system can be obtained in terms of the eigenspectrum of the Bogoliubov quasiparticles $\xi(\mathbf{k}) = \sqrt{E(\mathbf{k})^2 + |\Delta(\mathbf{k})|^2}$ as

$$\begin{aligned} F = -T \sum_{\mathbf{k}} \ln \left(1 + e^{-\beta \xi(\mathbf{k})} \right) - \frac{1}{2} \sum_{\mathbf{k}} (\xi(\mathbf{k}) - E(\mathbf{k})) \\ + \frac{1}{2} \sum_{\mathbf{k}} \frac{|\Delta(\mathbf{k})|^2}{2\xi(\mathbf{k})} \tanh \left(\frac{\xi(\mathbf{k})}{2T} \right). \end{aligned} \quad (17)$$

Its minimization w.r.t. the order parameter gives the BCS gap equation

$$\Delta(\mathbf{k}) = -\frac{1}{N} \sum_{\mathbf{k}'} \Gamma_P(\mathbf{k}, \mathbf{k}') \frac{\Delta(\mathbf{k}')}{2\xi(\mathbf{k}')} \tanh \left(\frac{\xi(\mathbf{k}')}{2T} \right). \quad (18)$$

Since the FRG flow breaks down at the onset of a phase transition, the appropriate temperature scale at the end of the flow is given by T_C , which implies $\Delta \rightarrow 0$. Thus, the righthand side of the above equation can be expanded to first order in the order parameter. From the linearised version of Eq. (18),

$$\lambda \Delta(\mathbf{k}) = \frac{1}{N} \sum_{\mathbf{k}'} \Gamma_P(\mathbf{k}, \mathbf{k}') \Delta(\mathbf{k}'), \quad (19)$$

the spatial dependence of the order parameter is given by

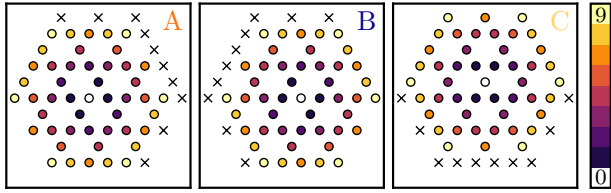


FIG. 7. Resymmetrization of formfactor expansion. When calculating in proper gauge we implicitly mix different distances in the truncation of the formfactor expansion in Eq. 9. To circumvent the thereby induced symmetry breaking, the formfactor basis has to be adjusted for each sublattice individually to suffice the site symmetry group C_{2v} . Sites x do not have a symmetry partner w.r.t the central site and are therefore discarded.

the eigenstate of Γ_P associated with the most negative eigenvalue λ . In the case of degenerate leading pairing eigenvalues, the system will realise the complex superposition of the degenerate modes, that minimizes the free energy in Eq. (17).

Vertex symmetrization routine

For computational convenience, the FRG treatment of the effective vertex is usually performed in proper gauge as describe in Ref. [17]: To maintain a periodic Hamiltonian w.r.t. the reciprocal lattice vectors, we choose a gauge where all sites o within the unit cell ($o \in \{A, B, C\}$) are transformed respective the origin of the unit cell

$$c_{i,o} = \int_{\text{BZ}} d\mathbf{k} e^{i\mathbf{k}\mathbf{r}_i} c_{\mathbf{k},o}, \quad (20)$$

with $\mathbf{r}_i = n\mathbf{a}_0 + m\mathbf{a}_1$, and $n, m \in \mathbb{Z}$ as opposed to the improper and non-periodic form

$$c_{i,o} = \int_{\text{BZ}} d\mathbf{k} e^{i\mathbf{k}(\mathbf{r}_i + \mathbf{r}_o)} c_{\mathbf{k},o}, \quad (21)$$

where they are transformed respective their position. \mathbf{r}_o denotes the shift from the unit cell origin to the position of sublattice o . Thus, $(\mathbf{r}_i + \mathbf{r}_o)$ are all lattice vectors of the Kagome lattice. The formfactor expansion in Equation 9 considers only a finite number of formfactors, which is defined by the number of formfactor shells (n_{shell}) around the onsite unit cell. This induces a truncation of neighboring real-space sites $\{\mathbf{r}_i : |\mathbf{r}_i| \leq d_n\}$, where d_n is the distance between onsite- and n_{shell} -NN unit cell. This is sufficient for intra-orbital terms. However, for inter-orbital contributions the different sublattice positions \mathbf{r}_o within a unit cell mix differing length scales [17]. Now $\exists \mathbf{r}_{i,o} : |\mathbf{r}_i + \mathbf{r}_o| > d_n$ and those elements break the symmetry of the system as the unit cell orientation favors one direction. An illustration of all sites contained in

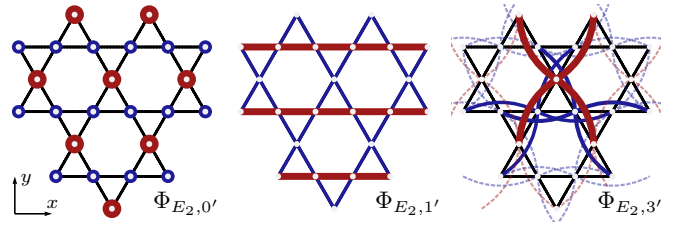


FIG. 8. Orthogonal complement of the onsite ($\Phi_{E_2,0'}$), nearest neighbor ($\Phi_{E_2,1'}$), and third nearest neighbor ($\Phi_{E_2,3'}$) pairing states presented in Figure 11 with y -mirror eigenvalue $+1$ (“even”). Red/blue indicates positive/negative value of the pair correlation between connected sites. The thickness of the lines symbolizes the magnitude of pair correlations (red: $+2$, blue: -1). For $\Phi_{E_2,3'}$ only the connections to the central unit cell are highlighted to preserve visual clarity.

the formfactor expansion up to third-NN unit cells can be found in Figure 7. To restore the symmetry we set elements that do not have a symmetry partner w.r.t. the central site (white) to zero in both, the scale derivatives of the propagators, and the effective interactions in each iteration of the FRG flow.

Complementing basis states of the E_2 irrep

In the main text the set of all lattice sites is referred to as ρ while subsets are denoted as ρ_i . With this we can define the lattice constraint factors $\delta_{\mathbf{R},\rho}$ as

$$\delta_{\mathbf{R},\rho} \equiv \sum_{n,m \in \mathbb{Z}} \sum_o \delta_{\mathbf{R},n\mathbf{a}_0 + m\mathbf{a}_1 + \mathbf{r}_o}, \quad (22)$$

where \mathbf{r}_o with $o \in A, B, C$ denotes the positions of the atoms A, B and C in the unit cell with $n, m \in \mathbb{Z}$. The subset of one type of sublattice thus follows as

$$\delta_{\mathbf{R},\rho_o} \equiv \sum_{n,m \in \mathbb{Z}} \delta_{\mathbf{R},n\mathbf{a}_0 + m\mathbf{a}_1 + \mathbf{r}_o}. \quad (23)$$

Another relevant subset consists of the corresponding closest centerpoints of a hexagon to a lattice site. We will denote it as $\rho_A \pm \delta_2$, $\rho_B \pm \delta_1$ and $\rho_C \pm \delta_0$, which are always the sites not present in the kagome lattice. For the A sites this results in

$$\delta_{\mathbf{R},\rho_A \pm \delta_2} \equiv \sum_{n,m \in \mathbb{Z}} \delta_{\mathbf{R},n\mathbf{a}_0 + m\mathbf{a}_1 + \mathbf{r}_A \pm \delta_2}. \quad (24)$$

The other two terms follow similarly. Various other subsets can be constructed in a similar fashion if needed. With this we are able to separate the inherent translation breaking of the kagome lattice via $\delta_{\mathbf{r}_k,\rho}$. The additional spatial structure induced by the emergent phase unveils the character of the instability. In the main text we chose the mirror symmetry along the y -axis as a tool to differ-

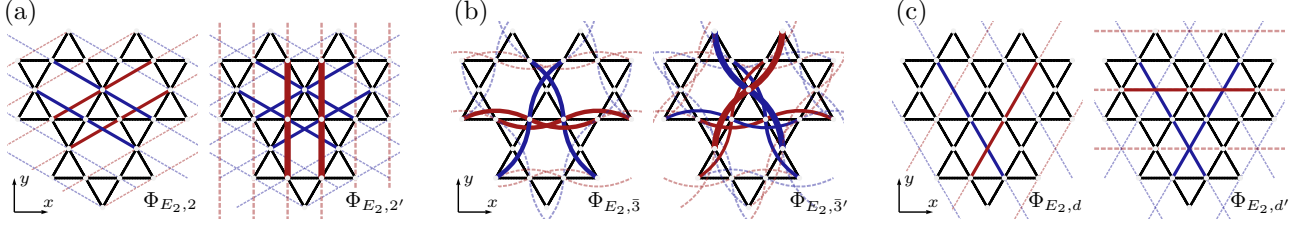


FIG. 9. Complementing E_2 pairing states of the kagome lattice up to third nearest-neighbor. (a) Next nearest-neighbor pairing states with odd ($\Phi_{E_2,2}$) and even ($\Phi_{E_2,2'}$) transformation property w.r.t. a y -mirror. (b) and (c) correspond to third nearest-neighbor pairing states whereas ($\Phi_{E_2,3}$) and ($\Phi_{E_2,3'}$) are formed by connections along the chains of the lattice while ($\Phi_{E_2,d}$) and ($\Phi_{E_2,d'}$) establish a link across the hexagons. Red/blue indicates the sign (+/-) for the pair correlation. The magnitude of pair correlations (± 1 or ± 2) is symbolized by the thickness of the lines. Connections to the central unit cell are highlighted for visual clarity.

entiate the two degenerate states transforming under the E_2 irrep. In detail, this mirror symmetry maps all C sites onto themselves while A and B sites are switched. From this, one can determine two additional symmetry operations that could equally have been chosen for our classification, namely $A \leftrightarrow C$ or $B \leftrightarrow C$. Since they are symmetry equivalent it suffices to only consider one of them.

Harmonic expansion of the E_2 sector

In this section we show the orthogonal states corresponding to the ones displayed in the main paper and complement these with the remaining states transforming under the E_2 irrep up to third nearest neighboring sites. A detailed analysis of their contributions is given which validates our restriction to Φ_{E_0} and Φ_{E_3} as the main contributions of the FRG state. The next nearest neighbor correlation state

$$\Phi_{E_2,2}(\mathbf{R}, \mathbf{r}) = \delta_{\mathbf{r},\pm(\delta_0+\delta_1)} - \delta_{\mathbf{r},\pm(\delta_0-\delta_2)}, \quad (25)$$

is structurally similar to $\Phi_{E_2,1}$, since it only consists of a relative coordinate (RC) dependence due to the center of mass coordinate (CMC) being already accounted for by the lattice constraint. In the third nearest neighbor shell, the number of sites exceeds the rank of the point group, which promotes two additional types of third nearest neighbor states:

$$\begin{aligned} \Phi_{E_2,3}(\mathbf{R}, \mathbf{r}) &= \delta_{\mathbf{R},\rho_B} \delta_{\mathbf{r},\pm\mathbf{a}_0} + \delta_{\mathbf{R},\rho_A} \delta_{\mathbf{r},\pm\mathbf{a}_0} \\ &\quad - \delta_{\mathbf{R},\rho_C} (\delta_{\mathbf{r},\pm\mathbf{a}_1} + \delta_{\mathbf{r},\pm\mathbf{a}_2}). \end{aligned} \quad (26)$$

is symmetric under a mirror operation along the y -axis and thus perpendicular to $\Phi_{E_2,3}$. The second state

$$\Phi_{E_2,d}(\mathbf{R}, \mathbf{r}) = \delta_{\mathbf{R},\rho_A \pm \delta_2} \delta_{\mathbf{r},\pm\mathbf{a}_2} - \delta_{\mathbf{R},\rho_B \pm \delta_1} \delta_{\mathbf{r},\pm\mathbf{a}_1}. \quad (27)$$

is not symmetry equivalent to the $\Phi_{E_2,3}$ and $\Phi_{E_2,3'}$ states since the CMC coordinate always lies in the hexagon center of the kagome lattice, i.e. an empty site. Due to this we call it the E_2,d where the d stands for *diagonal*. Another difference to the $\Phi_{E_2,3}/\Phi_{E_2,3'}$ states, is that the pairing sites have two intermediate sites as opposed to one, which decreases the relative contribution of the $\Phi_{E_2,d}$ state. The associated states with opposite transformation behavior under mirroring along the y -axis complete the basis set for the E_2 . These will be denoted by $\Phi_{E_2,i'}$. For the onsite state $\Phi_{E_2,0}$ we get

$$\Phi_{E_2,0'}(\mathbf{R}, \mathbf{r}) = \delta_{\mathbf{r},\mathbf{0}} \left(+ 2\delta_{\mathbf{R},\rho_C} - \delta_{\mathbf{R},\rho_B} - \delta_{\mathbf{R},\rho_A} \right). \quad (28)$$

The corresponding orthogonal states to $\Phi_{E_2,1}$ and $\Phi_{E_2,2}$ read

$$\begin{aligned} \Phi_{E_2,1'}(\mathbf{R}, \mathbf{r}) &= 2\delta_{\mathbf{r},\pm\delta_0} - \delta_{\mathbf{r},\pm\delta_1} - \delta_{\mathbf{r},\pm\delta_2}, \\ \Phi_{E_2,2'}(\mathbf{R}, \mathbf{r}) &= 2\delta_{\mathbf{r},\pm(\delta_1+\delta_2)} - \delta_{\mathbf{r},\pm(\delta_0+\delta_1)} - \delta_{\mathbf{r},\pm(\delta_0-\delta_2)}. \end{aligned} \quad (29)$$

The $\Phi_{E_2,3'}$ state, which transforms even under mirroring along the y -axis, has the same properties as its orthogonal counterpart in that it does not factorize into CMC and RC components

$$\begin{aligned} \Phi_{E_2,3'}(\mathbf{R}, \mathbf{r}) &= + 2 (\delta_{\mathbf{R},\rho_A} \delta_{\mathbf{r},\pm\mathbf{a}_1} + \delta_{\mathbf{R},\rho_B} \delta_{\mathbf{r},\pm\mathbf{a}_2}) \\ &\quad - (\delta_{\mathbf{R},\rho_C} \delta_{\mathbf{r},\pm\mathbf{a}_2} + \delta_{\mathbf{R},\rho_A} \delta_{\mathbf{r},\pm\mathbf{a}_0}) \\ &\quad - (\delta_{\mathbf{R},\rho_B} \delta_{\mathbf{r},\pm\mathbf{a}_0} + \delta_{\mathbf{R},\rho_C} \delta_{\mathbf{r},\pm\mathbf{a}_1}). \end{aligned} \quad (31)$$

The same holds for $\Phi_{E_2,3'}$

$$\begin{aligned} \Phi_{E_2,3'}(\mathbf{R}, \mathbf{r}) &= + 2 (\delta_{\mathbf{R},\rho_A} \delta_{\mathbf{r},\pm\mathbf{a}_1} - \delta_{\mathbf{R},\rho_B} \delta_{\mathbf{r},\pm\mathbf{a}_2}) \\ &\quad - (\delta_{\mathbf{R},\rho_C} \delta_{\mathbf{r},\pm\mathbf{a}_2} - \delta_{\mathbf{R},\rho_A} \delta_{\mathbf{r},\pm\mathbf{a}_0}) \\ &\quad - (\delta_{\mathbf{R},\rho_B} \delta_{\mathbf{r},\pm\mathbf{a}_0} - \delta_{\mathbf{R},\rho_C} \delta_{\mathbf{r},\pm\mathbf{a}_1}), \end{aligned} \quad (32)$$

which transforms odd under a mirror operation along the y -axis. Lastly we have the even counterpart to $\Phi_{E_2,d}$

$$\begin{aligned} \Phi_{E_2,d}(\mathbf{R}, \mathbf{r}) = & + 2\delta_{\mathbf{R},\rho_C \pm \delta_0} \delta_{\mathbf{r}, \pm \mathbf{a}_0} \\ & - \delta_{\mathbf{R},\rho_B \pm \delta_1} \delta_{\mathbf{r}, \pm \mathbf{a}_1} \\ & - \delta_{\mathbf{R},\rho_A \pm \delta_2} \delta_{\mathbf{r}, \pm \mathbf{a}_2}. \end{aligned} \quad (33)$$

which also does not factorize into CMC and RC. The real space representations of the states are shown in Figure 8, Figure 9.

Analyzing instabilities in the extended zone scheme

Extended zone scheme

The conventional approach to a structure with sublattice degree of freedom is to treat the modulations periodic with the Bravais vectors in reciprocal space within the corresponding BZ, while the sublattice structure is captured in an additional orbital degree of freedom. Despite this approach is favourable for both analytical and numerical calculations, it introduces an imbalance between intra- and inter-unit cell modulations. To remedy this shortcoming, one can reinterpret the Kagome lattice as an 1/4 depleted triangular lattice with half the lattice constant. The reciprocal lattice vectors double, and therefore the BZ quadruple in size, consequently encoding the full spatial information of the sublattice without the introduction of additional (orbital) degrees of freedom. We refer to this enlarged BZ as the *extended* BZ (eBZ). Wave vectors within this eBZ carry the whole spatial information of the basis sites, as it is also probed in experimental setups. In contrast to a Bravais lattice with point group C_{6v} , the eBZ takes into account the full space group of the Kagome lattice, which includes *e.g.* a glide reflection (translation of half a Bravais vector and subsequent inversion at this line). Breaking of this symmetry will lead to finite Q signals in experiments as discussed below.

To establish direct contact with the experiment and also gain deeper insight into the real space structure of the superconducting pairing wave function, one has to transfer the sublattice information from the sublattice degrees to the eBZ of the spatially fully resolved lattice. Since both perspectives encode the same information about the system, they are connected by a unitary transformation, that we will establish in the following.

Unfolding susceptibilities into the eBZ

To exemplify the transformation to the extended BZ utilising a momentum space picture, we consider the fol-

lowing particle-particle susceptibility

$$\begin{aligned} \Pi_{\{o_i\}}^{ff'}(\mathbf{Q}) = & \frac{1}{N} \sum_{\mathbf{k}, \mathbf{k}'} \varphi_f(\mathbf{k}) \varphi_{f'}^*(\mathbf{k}') \\ & \left\langle c_{\mathbf{k}+\mathbf{Q}, o_2}^\dagger c_{-\mathbf{k}, o_3}^\dagger c_{-\mathbf{k}', o_1} c_{\mathbf{k}'+\mathbf{Q}, o_0} \right\rangle \end{aligned} \quad (34)$$

as the outcome of our TUFGR analysis. The secondary momentum dependence in \mathbf{k} and \mathbf{k}' was expanded in a series of suitable formfactors $\varphi_f(\mathbf{k})$. As outlined in a previous section, this quantity is most conveniently obtained for a triangular lattice with tri-atomic basis in the natural gauge [16, 17], which encapsulates all information about the real space position of the sublattices relative to the unit-cell origin in orbital-like indices $o \in \{A, B, C\}$. To reconstruct the spacial information in the momentum domain and establish a link to experimental probes for the superconducting gap function, one has to apply the gauge transformation

$$c_{\mathbf{k}, o} \rightarrow c_{\mathbf{k}, o} e^{i\mathbf{k}\gamma_o}, \quad (35)$$

which respects the actual positions of the sublattices γ_o corresponding to the sublattice site o . Since the crystal momentum in Eq. 34 is defined with respect to the triangular superlattice, the phase winding introduced by the sublattice positions γ_i is not periodic in the initial but in the extended BZ. However, the Kagome lattice does not feature the full periodicity in the triangular lattice vectors $\delta_0 = \mathbf{a}_0/2$ and $\delta_1 = \mathbf{a}_1/2$, since 1/4 of the lattice sites remain empty. This reduced symmetry allows a finite support in the extended BZ only for harmonic functions without occupation on the vacant sites. This is equivalent to a FT of a triangular lattice of half the spacing with a nontrivial structure factor as known from diffraction experiments [?]. Applying the gauge transformation of Eq. 35 to the inverse of Eq. 34 and expanding the result in a set of formfactors adapted to the extended BZ $\varphi_g(\mathbf{k})$, one obtains

$$\Pi^{gg'}(\mathbf{Q}) = \sum_{f, f'} \sum_{\{o_i\}} e^{i\mathbf{Q}(\gamma_{o_0} - \gamma_{o_2})} \Pi_{\{o_i\}}^{ff'}(\mathbf{Q}) T_{\{o_i\}}^{gg'ff'} \quad (36)$$

with the momentum independent transformation matrix

$$\begin{aligned} T_{\{o_i\}}^{gg'ff'} = & \sum_{\mathbf{k}, \mathbf{k}'} e^{i\mathbf{k}(\gamma_{o_3} - \gamma_{o_2})} e^{i\mathbf{k}'(\gamma_{o_0} - \gamma_{o_1})} \\ & \phi_g(\mathbf{k}) \phi_{g'}^*(\mathbf{k}') \varphi_f^*(\mathbf{k}) \varphi_{f'}(\mathbf{k}'). \end{aligned} \quad (37)$$

This susceptibility presents the full Fourier transformed SC pairing susceptibility, that can be directly probed in Josephson STM measurements with a superconducting tip [30? , 31]. It encodes all information about the spatial ordering in the momentum distribution and emerges from the convolution of the orbital dependent susceptibility $\Pi_{\{o_i\}}^{ff'}(\mathbf{Q})$ with the atomic structure factor

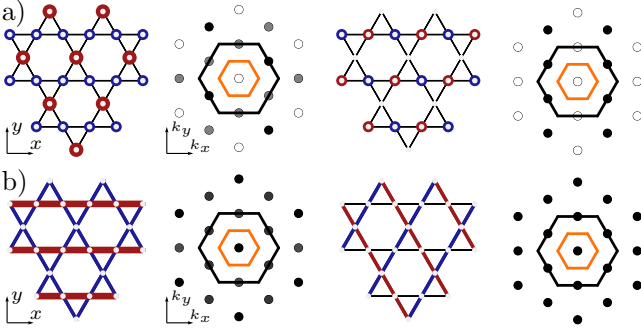


FIG. 10. Intra unit cell particle-particle instabilities transforming under the E_2 irreducible representation. Considering only pairing of electrons up to the nearest neighboring sites, the number of pairing functions within the E_2 irreducible representations of the onsite pairing states leading to a SMS order. b) represents the nearest neighbor bond order state correspond to a d -wave superconductor. Red (blue) sites (bonds) encode a positive (negative) value of the real valued gap function. While both orders reside at $\mathbf{Q} = 0$ in the reduced BZ (orange), they can be distinguished in the extended BZ (black).

$e^{i\mathbf{Q}(\gamma_{o_0} - \gamma_{o_2})}$. An analogous procedure can be applied to particle-hole susceptibilities to characterise magnetic and charge ordering.

Apparently, both descriptions are equivalent, since they only involve a gauge transformation. This can be easily understood by choosing plane wave formfactors $\varphi_f(\mathbf{k}) = e^{i\mathbf{k}\boldsymbol{\rho}_f}$ with $\boldsymbol{\rho}_f$ a real space lattice vector. Upon reducing the unit cell to a single site, the number of formfactors with finite support n_g is equivalent to the number of sublattice positions in the original unit cell n_o times the number of previously employed formfactors n_f . We therefore see, that the intra-unit cell degrees of freedom are faithfully transferred to the corresponding momentum structure without any loss of information. Assuming

$$\varphi_f(\mathbf{k}) = e^{-i\mathbf{k}\mathbf{R}_f} \quad \phi_g(\mathbf{k}) = e^{-i\mathbf{k}\mathbf{r}_g} \quad (38)$$

we find

$$\begin{aligned} t_{o_2 o_3}^{fg} &= \delta(\delta_3 - \delta_2 - \mathbf{r}_g + \mathbf{R}_f) \\ t_{o_0 o_1}^{f'g'} &= \delta(\delta_0 - \delta_1 - \mathbf{R}_{f'} + \mathbf{r}_{g'}), \end{aligned} \quad (39)$$

and clearly

$$T_{\{o_i\}}^{gg'ff'} = t_{o_2 o_3}^{fg} t_{o_0 o_1}^{f'g'}, \quad (40)$$

i.e. T confines contributing formfactors to the actually occupied sites in the real space lattice structure.

As discussed in the main text, there are two ways to achieve a pairing structure in the Kagome lattice, which follows d -wave symmetries. As for any lattice, a nearest neighbor pairing with suitable amplitudes can be constructed. However, because of the three basis points within one Kagome unit-cell arranged in a $3/4$ depleted triangular lattice, there exist an additional possibility of having a modulation in the on-site pairing amplitude without disrupting the translational symmetry of the underlying Bravais lattice. In the conventional reduced zone scheme, both states therefore will feature an ordering vector at the Γ point.

The first choice, as expected from a superconducting state, is completely uniform along all direction of the nearest neighbor bonds, while the latter clearly is not. This will result in an ordering vector away from Γ in the extended zone scheme. To illustrate this, compare the two states with $(-1, -1, 2)$ modulation as depicted in Figure 10. The real-space pairing is given by Eq. (28) for the modulated on-site pairing and Eq. (30) for the translationally invariant nearest-neighbor pairing. Let us first consider the momentum structure of these pairings in the reduced scheme, given by

$$\begin{aligned} \Phi^{o_0 o_1}(\mathbf{Q}, \mathbf{k}) &= \sum_{\mathbf{r}_0, \mathbf{r}_1} \Phi(\mathbf{r}_0, \mathbf{r}_1) e^{-i\mathbf{Q}(\mathbf{r}_0 - \delta_{o_0} + \mathbf{r}_1 - \delta_{o_1})/2} \\ &\quad e^{-i\mathbf{k}(\mathbf{r}_1 - \delta_{o_1} - \mathbf{r}_0 + \delta_{o_0})}. \end{aligned} \quad (41)$$

Substituting (28), we find

$$\begin{aligned} \Phi_{E_2, 0'}^{o_0 o_1}(\mathbf{Q}, \mathbf{k}) &= \sum_{\mathbf{R}_0, \mathbf{R}_1} \delta_{\mathbf{R}_0, \mathbf{R}_1} \delta_{o_0, o_1} e^{-i\mathbf{Q}(\mathbf{R}_0 + \mathbf{R}_1)/2} \\ &\quad (-\delta_{o_0, 0} - \delta_{o_0, 1} + 2\delta_{o_0, 2}), \end{aligned} \quad (42)$$

where \mathbf{R}_i are the Bravais vectors of the unit cell \mathbf{r}_i resides in. Using the completeness of lattice Fourier transforms, this simplifies to

$$\begin{aligned} \Phi_{E_2, 0'}^{o_0 o_1}(\mathbf{Q}, \mathbf{k}) &= \delta_{o_0, o_1} (-\delta_{o_0, 0} - \delta_{o_0, 1} + 2\delta_{o_0, 2}) \delta_{\mathbf{Q}, \mathbf{G}} \\ &= \begin{pmatrix} -1 & 0 & 0 \\ 0 & -1 & 0 \\ 0 & 0 & 2 \end{pmatrix} \delta_{\mathbf{Q}, \mathbf{G}} \end{aligned} \quad (43)$$

with a reciprocal lattice vector \mathbf{G} of the Kagome lattice. Within the BZ, therefore, this gap function has support only at $\mathbf{Q} = \Gamma$, with uniform distribution in \mathbf{k} . Repeating the same procedure for Δ_{dSC} we find

$$\begin{aligned} \Phi_{E_2, 1'}^{o_0 o_1}(\mathbf{Q}, \mathbf{k}) &= \delta_{\mathbf{Q}, \mathbf{G}} \\ &\quad \begin{pmatrix} 0 & 2(1 + e^{-i\mathbf{k}\mathbf{a}_1}) & -(1 + e^{-i\mathbf{k}\mathbf{a}_2}) \\ 2(1 + e^{i\mathbf{k}\mathbf{a}_1}) & 0 & -(1 + e^{i\mathbf{k}(\mathbf{a}_1 - \mathbf{a}_2)}) \\ -(1 + e^{i\mathbf{k}\mathbf{a}_2}) & -(1 + e^{-i\mathbf{k}(\mathbf{a}_1 - \mathbf{a}_2)}) & 0 \end{pmatrix}, \end{aligned} \quad (44)$$

again with support only at $\mathbf{Q} = \Gamma$ within the BZ but now with a structure in k .

Shifting to the eBZ picture, we have to take the real-space positions of the basis points into consideration. The gap function in this representation in reciprocal space is given by

$$\begin{aligned}\Phi(\mathbf{Q}, \mathbf{k}) &= \sum_{\mathbf{r}_0, \mathbf{r}_1} \Phi(\mathbf{r}_0, \mathbf{r}_1) e^{-i\mathbf{Q}(\mathbf{r}_0 + \mathbf{r}_1)/2} e^{-i\mathbf{k}(\mathbf{r}_1 - \mathbf{r}_0)} \\ &= \sum_{o_0, o_1} \Phi^{o_0 o_1}(\mathbf{Q}, \mathbf{k}) e^{-i\mathbf{Q}(\delta_{o_0} + \delta_{o_1})/2} e^{-i\mathbf{k}(\delta_{o_0} - \delta_{o_1})}\end{aligned}\quad (45)$$

according to Eq. 36. Consequently, the eBZ expression for the on-site pairing is given by

$$\Phi_{E_2, 0'}(\mathbf{Q}, \mathbf{k}) = (-1 - e^{-i\mathbf{Q}\delta_0} + 2e^{-i\mathbf{Q}\delta_1})\delta_{\mathbf{Q}, \mathbf{G}}. \quad (46)$$

Because, in the Kagome lattice the sublattice vectors $\delta_i = \mathbf{a}_i/2$ are half of the Bravais vectors, the phase factors will result in multiples of π for the reciprocal lattice points, such that there will be support on the M points of the eBZ, but not at Γ .

For the uniform state, in contrast, we find

$$\begin{aligned}\Phi_{E_2, 1'}(\mathbf{Q}, \mathbf{k}) &= (2 \cos(\mathbf{k}\delta_0) e^{-i\mathbf{Q}\delta_0/2} \\ &\quad - \cos(\mathbf{k}\delta_1) e^{-i\mathbf{Q}\delta_1/2} \\ &\quad - \cos(\mathbf{k}(\delta_0 - \delta_1)) e^{-i\mathbf{Q}(\delta_0 - \delta_1)/2}) \delta_{\mathbf{Q}, \mathbf{G}}.\end{aligned}\quad (47)$$

While this state also features some dependence on the relative momentum \mathbf{k} of the Cooper pair constituents, for fixed \mathbf{k} the phases associated with the Cooper pair momentum \mathbf{Q} are not able to destructively interfere in order to suppress a peak in the eBZ. This results in the distinct \mathbf{Q} map of the SMS and d SC phase depicted in Figure 10. Variations in gap size as well as the phase difference of the superconducting order parameter could be probed at atomic scale within experiments using phase sensitive superconducting STM techniques [32].

CANDIDATE STATE ANALYSIS OF FRG RESULTS

In order to trace the competing contributions within the FRG flow, i.e. as a function of energy cutoff Λ , we determine the expectation value

$$\Xi = \langle \Phi_{\nu, \theta} | V_{\nu} | \Phi_{\nu, \theta} \rangle \quad (48)$$

of the effective FRG vertex V_{ν} at each flow step. $\nu \in (\text{pp}, \text{cha}, \text{mag})$ denotes the physical instability channels reconstructed from the TUFrg decomposition in Eq. (13), (14), (15). θ defines the candidate state, for which we take the final FRG state of the respective

phases.

To calculate the overlaps of the FRG state with the candidate states we define

$$\gamma_{E_2, i} = |\langle \Psi_{\text{FRG}} | \Phi_{E_2, i} \rangle|^2 + |\langle \Psi_{\text{FRG}} | \Phi_{E_2, i'} \rangle|^2. \quad (49)$$

As shown in Table I, the FRG state is predominantly composed of $\Phi_{E_2, 0}$ and $\Phi_{E_2, 3}$. When increasing the nearest-neighbor repulsion V , the ratio $\Phi_{E_2, 3}/\Phi_{E_2, 0}$ declines as longer-ranged fluctuations are suppressed. To highlight this fact we define the ratio

$$\alpha = \frac{1}{2} + \frac{1}{2} \frac{\gamma_{E_2, 0} - \gamma_{E_2, 3}}{\gamma_{E_2, 0} + \gamma_{E_2, 3}} \quad (50)$$

resulting in $\alpha = 0$ ($\alpha = 1$) for a pure $\Phi_{E_2, 3}$ ($\Phi_{E_2, 0}$) contribution.

V/t	$\gamma_{E_2, 0}$	$\gamma_{E_2, 1}$	$\gamma_{E_2, 2}$	$\gamma_{E_2, 3}$	$\gamma_{E_2, d}$	$\gamma_{E_2, \bar{3}}$	γ_{A_1}	Σ
0.50	50.86	0.00	0.55	43.76	0.11	0.01	0.0	95.31
0.52	53.75	0.00	0.60	41.47	0.04	0.01	0.0	95.87
0.54	56.13	0.00	0.63	39.44	0.01	0.01	0.0	96.23
0.56	58.18	0.00	0.66	37.63	0.00	0.01	0.0	96.49
0.58	59.95	0.00	0.69	36.02	0.00	0.01	0.0	96.68
0.60	61.53	0.00	0.72	34.57	0.01	0.01	0.0	96.84
0.62	62.92	0.00	0.74	33.25	0.03	0.01	0.0	96.97
0.64	64.18	0.00	0.77	32.05	0.06	0.02	0.0	97.07
0.66	65.29	0.01	0.80	30.96	0.09	0.02	0.0	97.16
0.68	66.30	0.01	0.82	29.95	0.13	0.02	0.0	97.22
0.70	0.0	0.0	0.0	0.0	0.0	0.0	80.21	80.21
0.72	0.0	0.0	0.0	0.0	0.0	0.0	80.82	80.82

TABLE I. Overlap of the final FRG state (pp channel) with candidate states at $U = 0.14$ in percent. Values are calculated according to Equation 49.

SMS Mean field results

In the case of the onsite E_2 states, dominating the SMS domain, the free energy is minimized within the MF approximation by the chiral superposition of $\Phi_{E_2, 0(\prime)}$ depicted in Fig. 11a). This leads to a phase winding of 4π within each hexagon with equal weights on the sublattices. The phases are transferred to the peak structure within the eBZ in Fig. 11b). While the absolute values restore the hexagonal symmetry, the phase modulation along each kagome chain still results in a finite Cooper pair momentum with respect to the single-site unit cell. This linear combination of degenerate E_2 states fully gaps the FS with larger values at the M points, where density of states accumulates. The gap structure is almost identical to that of a chiral d -wave SC, which omitted a correct identification of the SMS state in previous works [21]. As outlined before, the modulation of the phase can be probed within STMs with superconducting tips [32], enabling the distinction between ordinary su-

perconductors and the proposed new type of SMS.

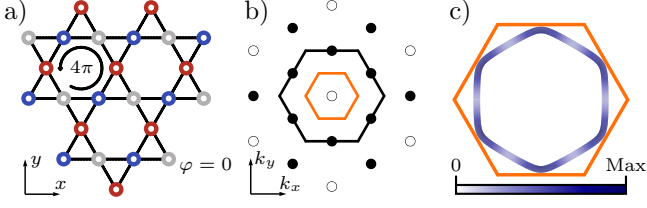


FIG. 11. Kagome sublattice modulated SC (SMS) order at $U/t=1.0$, $V/t=1.1$. The SMS state is dominated by on-site correlations that display a phase modulation in the unit cell as shown in a). The phase of the local order parameter $\Phi(\mathbf{R}_S, \mathbf{0})$ is indicated by the color of the dots where blue (red) represents $\varphi = 2\pi/3$ ($\varphi = -2\pi/3$) and white depicts $\varphi = 0$. The absolute value is identical for all points. The representation in the extended zone scheme in b) coincides with the expected \mathbf{k} space patterns accessible in STM measurements. c) shows the absolute value of the SMS gap on the FS.